PROGRESS REPORT

Meshfree Modeling of Munitions Penetration in Soils - Year 1

SERDP Project MR-2628

DECEMBER 2019

Sheng-Wei Chi
University of Illinois at Chicago

SERDP
DOD ▪ EPA ▪ DOE

REPORT DOCUMENTATION PAGE

Form Approved
OMB No. 0704-0188

1. REPORT DATE *(DD-MM-YYYY)*	**2. REPORT TYPE**	**3. DATES COVERED** *(From - To)*
31/12/2019	SERDP Progress Report	9/28/2018 - 9/28/2021

4. TITLE AND SUBTITLE

Meshfree Modeling of Munitions Penetration in Soils - Year 1

5a. CONTRACT NUMBER
18-C-0099

5b. GRANT NUMBER

5c. PROGRAM ELEMENT NUMBER

6. AUTHOR(S)
Sheng-Wei Chi

5d. PROJECT NUMBER
MR-2628

5e. TASK NUMBER

5f. WORK UNIT NUMBER

7. PERFORMING ORGANIZATION NAME(S) AND ADDRESS(ES)
University of Illinois at Chicago
Civil and Materials Engineering
842 W. Taylor Street
3087 Engineering Research Facility
Chicago, IL 60607-7023

8. PERFORMING ORGANIZATION REPORT NUMBER
MR-2628

9. SPONSORING/MONITORING AGENCY NAME(S) AND ADDRESS(ES)
Strategic Environmental Research and Development Program (SERDP)
4800 Mark Center Drive, Suite 16F16
Alexandria, VA 22350-3605

10. SPONSOR/MONITOR'S ACRONYM(S)
SERDP

11. SPONSOR/MONITOR'S REPORT NUMBER(S)
MR-2628

12. DISTRIBUTION/AVAILABILITY STATEMENT
DISTRIBUTION STATEMENT A. Approved for public release: distribution unlimited.

13. SUPPLEMENTARY NOTES

14. ABSTRACT
The objective of this project is to develop physically-based models to predict the penetration depth of common military munitions in various soil conditions. Ultimately, the models will be used to determine probable depths of munitions in the soil of formerly used defense sites in support of planning for remediation. The simulation results can be used to aid sensor detection and removal of these munitions.

15. SUBJECT TERMS
Meshfree Modeling, Munitions Penetration, Soils

16. SECURITY CLASSIFICATION OF:			**17. LIMITATION OF ABSTRACT**	**18. NUMBER OF PAGES**	**19a. NAME OF RESPONSIBLE PERSON**
a. REPORT	**b. ABSTRACT**	**c. THIS PAGE**			Sheng-Wei Chi
UNCLASS	UNCLASS	UNCLASS	UNCLASS	41	**19b. TELEPHONE NUMBER** *(Include area code)* 312-996-5024

Table of Contents

List of Tables

List of Figures

Meshfree Modeling of Munitions Penetration in Soils

Sheng-Wei Chi, Craig Foster, Mohammed M. Atif, and Jianfei Tian

Department of Civil and Materials Engineering
University of Illinois at Chicago, Chicago, IL 60607
swchi@uic.edu

1. Project Objective

The objective of this project is to develop physically-based models to predict the penetration depth of common military munitions in various soil conditions. Ultimately, the models will be used to determine probable depths of munitions in the soil of formerly used defense sites in support of planning for remediation. The simulation results can be used to aid sensor detection and removal of these munitions.

2. Summary of Outcomes in the Reporting Year

- The quasi-linear Reproducing Kernel (RK) formulation was introduced and implemented in the two-field meshfree code for penetration into soil simulations. The new implementation ensures that the RK approximation can be constructed under extreme deformations without compromising solution accuracy.
- The gradient-based stabilization technique was developed and implemented in the code to enhance solution accuracy and stability when the nodal integration is used for the domain integration involved in the Galerkin procedure. The new stabilization does not require a tunable parameter.
- The absorbing boundary condition was introduced and implemented in the meshfree framework to minimize the reflected wave due to the unphysical boundaries of a truncated domain. It provides an efficient means to model the semi-infinite domain involved in penetration into earth simulations.
- Improvements were implemented in the soil constitutive model to more accurately capture soil behavior. The growth function for the cap surface was reformulated so that it better reproduces experimental data. Simulations show that inelastic compaction at high mean stresses is more accurately captured. The plastic potential function was also modified so that plastic compaction of the soil may occur even as the shear strength is increasing.
- Some algorithmic improvements were implemented so that the robustness and efficiency of the soil model were enhanced. Changes to the way that the tangent modulus is calculated have improved performance and speed. Numerical testing indicates optimal quadratic convergence over a wide range of parameter values and loading conditions.
- Soil tests and drop tests for silica sands were conducted to validate the numerical predictions. The numerical results capture the deformation features observed in the experiment. The errors of final depth are within 7%.
- 2 journal paper publications:

- Mahdavi, A., Chi, S.W., and Atif, M.M., "A two-field semi-Lagrangian reproducing kernel model for impact and penetration simulation into geo-materials," Computational Particle Mechanics, 2019 (In press). https://doi.org/10.1007/s40571-019-00253-0.
- Mahdavi, A., Chi, S.W., and Zhu, H., "A gradient reproducing kernel collocation method for high order differential equations," Computational Mechanics, 64(5):1421-1454, 2019. https://doi.org/10.1007/s00466-019-01724-0.

- 2 conference presentations:
  - Chi, S.W., Mahdavi, A., and Atif, M., "A Semi-Lagrangian Reproducing Kernel Approach for Simulation of Penetration into Geo-materials," USNCCM 2019, July 28-August 1, Austin, TX.
  - Chi, S.W., Mahdavi, A., and Atif, M., "A Semi-Lagrangian Reproducing Kernel Approach for Simulation of Penetration into Geo-materials," COMPLAS 2019, September 3-5, 2019, Barcelona, Spain.

3. Proposed Tasks in the Reporting Year

Tasks	**Start date**	**Due Date**
Task 1. Enhancement of Multi-field Meshfree Code		
1.1. Development and implementation of a multi-field enhanced nodal integration scheme	10/11/2018	3/31/2019
1.2. Development and implementation of stabilization for the nodally integrated mixed formulation	10/11/2018	3/31/2019
1.3. Verification for the development and implementation in Tasks 1.1 and 1.2	2/1/2019	6/30/2019
Task 2. Soil Constitutive Model Improvement		
2.1. Algorithm improvements	10/11/2018	3/31/2019
2.2. Implementation improvements	12/1/2018	3/31/2019
2.3. Verification for the development and implementation in Tasks 2.1 and 2.2	3/1/2019	6/30/2019
Task 3. Soil Tests and Drop Tests for Dry Sand		
3.1. Calibrate lab equipment and prepare soil sample	10/11/2018	12/31/2018
3.2. Tests for calibration of soil properties	1/1/2019	4/30/2019
3.3. Drop test for dry sand	5/1/2019	6/30/2019

4. Tasks Accomplished

4.1. Task 1: Enhancement of Multi-field Meshfree Implementation

4.1.1. Recap of Semi-Lagrangian RK Approximation

This section recapitulates the reproducing kernel (RK) approximation, which provides the main framework for meshfree simulations in this project. The purpose of the recap is to provide the necessary background to introduce the new enhancements that we developed and implemented in this reporting period.

The RK approximation of a function $u(\mathbf{x})$, constructed based on a set of points $\{\mathbf{x}_I\}_{I=1}^{NP}$, is expressed as:

$$u(\mathbf{x}) \approx \sum_{I=1}^{NP} \Psi_I(\mathbf{x}) d_I = \sum_{I=1}^{NP} C(\mathbf{x};\mathbf{x}-\mathbf{x}_I)\phi_a(\mathbf{x}-\mathbf{x}_I) d_I \tag{1}$$

where Ψ_I is the RK shape function associated with node *I* and d_I is the corresponding coefficient. $\phi_a(\mathbf{x}-\mathbf{x}_I)$ is the kernel function and $C(\mathbf{x};\mathbf{x}-\mathbf{x}_I)$ is the correction function introduced to ensure approximation accuracy up to the desired order, and it is usually expressed by the linear combination of a set of *m-th* order complete monomials, the vector form of which is denoted as $\mathbf{H}(\mathbf{x}-\mathbf{x}_I)$ in the following:

$$C(\mathbf{x};\mathbf{x}-\mathbf{x}_I) \equiv \mathbf{H}(\mathbf{x}-\mathbf{x}_I)\mathbf{b}(\mathbf{x}) \tag{2}$$

The coefficient $\mathbf{b}(\mathbf{x})$ can be determined by the reproducing condition (Guan *et al*., 2011; Chi *et al*., 2014; Chen *et al*. 2017). Subsequently, the RK shape function is given as follows.

$$\Psi_I(\mathbf{x}) = \mathbf{H}^T(\mathbf{0})\mathbf{M}^{-1}(\mathbf{x})\mathbf{H}(\mathbf{x}-\mathbf{x}_I)\phi_a(\mathbf{x}-\mathbf{x}_I) \tag{3}$$

where $\mathbf{M}(\mathbf{x})$, called the moment matrix, is expressed as:

$$\mathbf{M}(\mathbf{x}) = \sum_{I=1}^{NP} \mathbf{H}(\mathbf{x}-\mathbf{x}_I)\mathbf{H}^T(\mathbf{x}-\mathbf{x}_I)\phi_a(\mathbf{x}-\mathbf{x}_I) \tag{4}$$

It is noted that for $\mathbf{M}(\mathbf{x})$ to be invertible, any spatial point $\mathbf{x}$ in the domain must be covered by sufficient kernels, the amount of which depends on the order of accuracy and the spatial dimension (Chen *et al*. 2017).

4.1.2. Quasi-linear Reproducing Kernel Approximation

To ensure that the RK approximation is constructible and achieve the desired order, the necessary condition is to have sufficient kernel functions to cover any evaluation point in the problem domain. However, the condition may be difficult to achieve under extreme deformations involving fragmentations or material separation. To ensure that the moment matrix (4) is always invertible and the approximation achieves at least linear-order accuracy, the quasi-linear RK approximation (Yreux and Chen, 2017) is introduced in the meshfree formulation and implemented in the code.

An additional set of NQ sampling points is introduced in the derivation of RK approximation as shown in Figure 1. After imposing the reproducing kernel, the quasi-linear RK approximation takes the following form:

$$\tilde{\Psi}_I(\mathbf{x}) = \mathbf{H}^T(\mathbf{0})\tilde{\mathbf{M}}^{-1}(\mathbf{x})\tilde{\mathbf{H}}(\mathbf{x},\mathbf{x}_I)\phi_a(\mathbf{x}-\mathbf{x}_I) \tag{5}$$

where

$$\tilde{\mathbf{M}}(\mathbf{x}) = \mathbf{M}(\mathbf{x}) + \varpi\bar{\mathbf{M}}(\mathbf{x}) \tag{6}$$

$$\bar{\mathbf{M}}(\mathbf{x}) = \sum_{I=1}^{NP}\sum_{k=1}^{NQ}\mathbf{H}(\mathbf{x}-\bar{\mathbf{x}}_k(\mathbf{x}))\mathbf{H}^T(\mathbf{x}-\bar{\mathbf{x}}_k(\mathbf{x}))\phi_a(\mathbf{x}-\mathbf{x}_I) \tag{7}$$

In equation (6), ϖ is a pre-selected parameter, which is chosen as 0.1 in the numerical results, unless otherwise mentioned (Yreux and Chen, 2017).

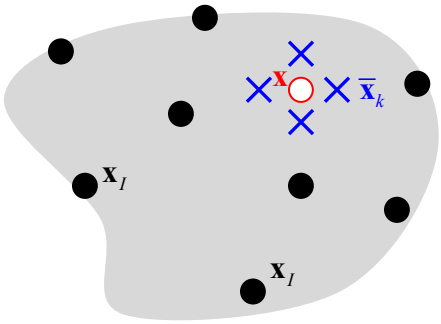

Figure 1. Schematic of additional sampling points for quasi-linear RK

4.1.3. Stabilization for Nodally Integrated Multi-Field Formulation

In the earlier version of the meshfree code, the Modified Stabilized Non-Conforming Nodal Integration (MSNNI) (Chen et al., 2006) was used, which provides effective stabilization to suppress spurious modes but requires a tunable parameter. The new stability for nodal integration (Hillman and Chen, 2016; Wu and Chi *et al*., 2016) was introduced for the multi-field formulation and implemented in the meshfree code. The stabilization is based on gradients of the strain field around the nodal point $\mathbf{x}_I$ as:

$$\boldsymbol{\varepsilon}(\mathbf{u}^h(\mathbf{x})) \approx \boldsymbol{\varepsilon}(\mathbf{u}^h(\mathbf{x}_I)) + (x-x_L)\boldsymbol{\varepsilon}(\partial_x\mathbf{u}^h(\mathbf{x}_I)) + (y-y_L)\boldsymbol{\varepsilon}(\partial_y\mathbf{u}^h(\mathbf{x}_I)) + (z-z_I)\boldsymbol{\varepsilon}(\partial_z\mathbf{u}^h(\mathbf{x}_I)). \tag{8}$$

The derivatives, $\partial_x\mathbf{u}^h$, $\partial_y\mathbf{u}^h$, and $\partial_z\mathbf{u}^h$, in equations (8) are approximated by implicit derivatives of RK approximation (Chen *et al*., 2004; Chi *et al*., 2013), which can be obtained much more efficiently than the direct derivatives of the RK. Substituting (8) for the strains near each integration node, the stabilized strain energy can be written as:

$$a_{ND}\langle\mathbf{v}^h,\mathbf{u}^h\rangle = a_D\langle\mathbf{v}^h,\mathbf{u}^h\rangle + a_N\langle\mathbf{v}^h,\mathbf{u}^h\rangle, \tag{9}$$

where $a_D\langle\cdot,\cdot\rangle$ is the standard nodally integrated strain energy:

$$a_D\langle \mathbf{v}^h, \mathbf{u}^h \rangle = \sum_{L=1}^{NP} \boldsymbol{\varepsilon}(\mathbf{v}^h(\mathbf{x}_I)) : \mathbf{C} : \boldsymbol{\varepsilon}(\mathbf{u}^h(\mathbf{x}_I)) W_L \,. \tag{10}$$

The additional stabilization term is:

$$a_N\langle \mathbf{v}^h, \mathbf{u}^h \rangle = \sum_{L=1}^{NP} \left\{ \boldsymbol{\varepsilon}(\hat{\mathbf{v}}_x^h) : \mathbf{C} : \boldsymbol{\varepsilon}(\hat{\mathbf{u}}_x^h) M_{Lx} + \boldsymbol{\varepsilon}(\hat{\mathbf{v}}_y^h) : \mathbf{C} : \boldsymbol{\varepsilon}(\hat{\mathbf{u}}_y^h) M_{Ly} + \boldsymbol{\varepsilon}(\hat{\mathbf{v}}_z^h) : \mathbf{C} : \boldsymbol{\varepsilon}(\hat{\mathbf{u}}_z^h) M_{Lz} \right\} \tag{11}$$

where M_{Lx}, M_{Ly}, and M_{Lz} are the second moments of inertia of the nodal domains about node L, which can be calculated explicitly. This stabilization scheme has been implemented in the multi-field formulation for soil penetration modeling.

4.1.4. Absorbing Boundary Condition

One of the issues in simulations of penetration into the earth is to effectively model the on-site environment, the domain of which is typically considered as semi-infinite. For efficiency, the computational domain is curtailed near the impact region, and special treatments are required on the curtailed boundaries to eliminate non-physical wave reflections. One of the most common ways to limit the non-physical reflected waves due to boundaries is through the implementation of absorbing boundary conditions. The absorbing boundary condition can be formulated as either a local type or a global type. Due to high computational costs for implementation of the global type of absorbing boundary condition, the local type is generally preferred. Considering that the penetration processes are highly transient and the spectrum of mechanical waves due to impact is very broad, the standard viscous boundary by Lysmer and Kuhlemeyer (1969) was selected and implemented. This boundary can be described by two series of dashpots oriented normal and tangential to the boundary. The advantage of this approach is that the absorption characteristics are independent of frequency and thus it is better suited for penetration simulations, in which broadband waves are generated.

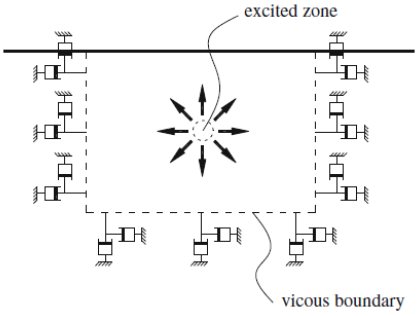

Figure 2. Schematic of the Lysmer and Kuhlemeyer boundary condition (standard viscous boundary condition)

The standard viscous boundary condition, as proposed by Lysmer and Kuhlemeyer (1969), is formulated in terms of the normal and tangential components of stress on the boundary as:

$$\begin{aligned} n + a\rho V_p \frac{\partial u}{\partial t} &= 0 \\ \tau + b\rho V_s \frac{\partial v}{\partial t} &= 0 \end{aligned} \quad \text{on the boundary } \Gamma_d \tag{12}$$

where V_p is the longitudinal velocity, V_s is the shear velocity, n is the normal stress, τ is the tangential stress, ρ is the density of the material, u and v are the displacements in the normal and tangential directions, respectively, and 'a' and 'b' are dimensionless parameters. The Galerkin formulation of the equilibrium equation is then:

$$\int_\Omega \mathbf{w} \cdot (\nabla \boldsymbol{\sigma} + \mathbf{f}_b) d\Omega = \int_\Omega \mathbf{w} \cdot \rho \ddot{\mathbf{u}} \, d\Omega \tag{13}$$

$$\int_\Omega \nabla \mathbf{w} \cdot \boldsymbol{\sigma} d\Omega + \int_\Omega \mathbf{w} \rho \ddot{\mathbf{u}} \, d\Omega = \int_\Omega \mathbf{w} \mathbf{f}_b d\Omega + \int_{\Gamma_c} \mathbf{w} \cdot (\mathbf{n} \cdot \boldsymbol{\sigma}) d\Gamma + \int_{\Gamma_d} \mathbf{w} \cdot (\mathbf{n} \cdot \boldsymbol{\sigma}) d\Gamma \tag{14}$$

$$\int_\Omega \nabla \mathbf{w} \cdot \boldsymbol{\sigma} d\Omega + \int_{\Gamma_d} w_u a V_p \frac{\partial u}{\partial t} d\Gamma + \int_{\Gamma_d} w_v b V_s \frac{\partial v}{\partial t} d\Gamma + \int_\Omega \mathbf{w} \cdot \rho \ddot{\mathbf{u}} \, d\Omega = \int_\Omega \mathbf{w} \cdot \mathbf{f}_b d\Omega + \int_{\Gamma_c} \mathbf{w} \cdot (\mathbf{n} \cdot \boldsymbol{\sigma}) d\Gamma \tag{15}$$

where $\boldsymbol{\sigma}$ is the Cauchy stress, $\mathbf{f}_b$ is the body force, and $\mathbf{w}$ is the test function.

4.1.5. Simulations of Absorbing Boundary Condition

The standard viscous boundary condition was implemented and verified in three different benchmark problems. In these problems, self-consistent unitless parameters are employed for the purpose of verification.

Problem 1: 1D case

Consider the equilibrium equation without the body force $\rho\ddot{u} = Eu_{,xx}$. The parameters $E = 1$, $\rho = 1$, and L=4, are selected. A half-sine impulse given in terms of velocity (Figure 4) is imposed as the initial conditions to generate an impulse wave. Boundary conditions and initial conditions are $\mathrm{u}(0,\mathrm{t}) = 0, \mathrm{u}(x,0) = 0, \mathrm{v}(0 < x < 0.5) = \sin\left(\frac{\pi x}{0.5}\right)$. The numerical solutions were carried out using the SCNI method for domain integration. The results in Figure 5 and Figure 6 show that the standard viscous boundary absorbs the impinging waves effectively. There are negligible waves reflected back to the problem domain.

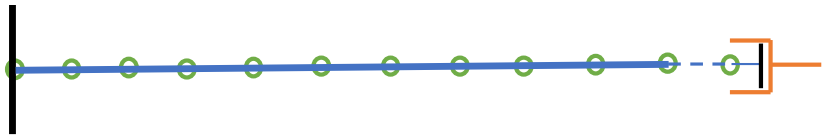

Figure 3. Schematic of a 1D beam with a damper at the right end

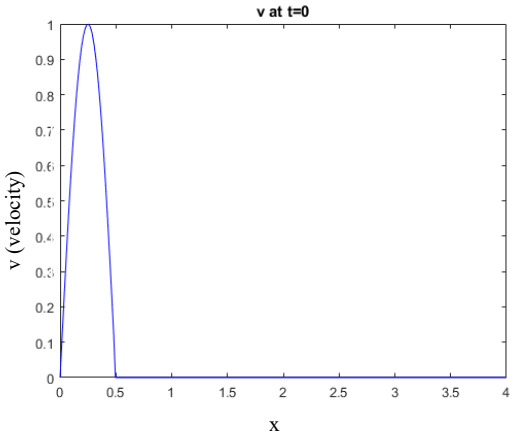

Figure 4. Initial velocity imposed to the beam

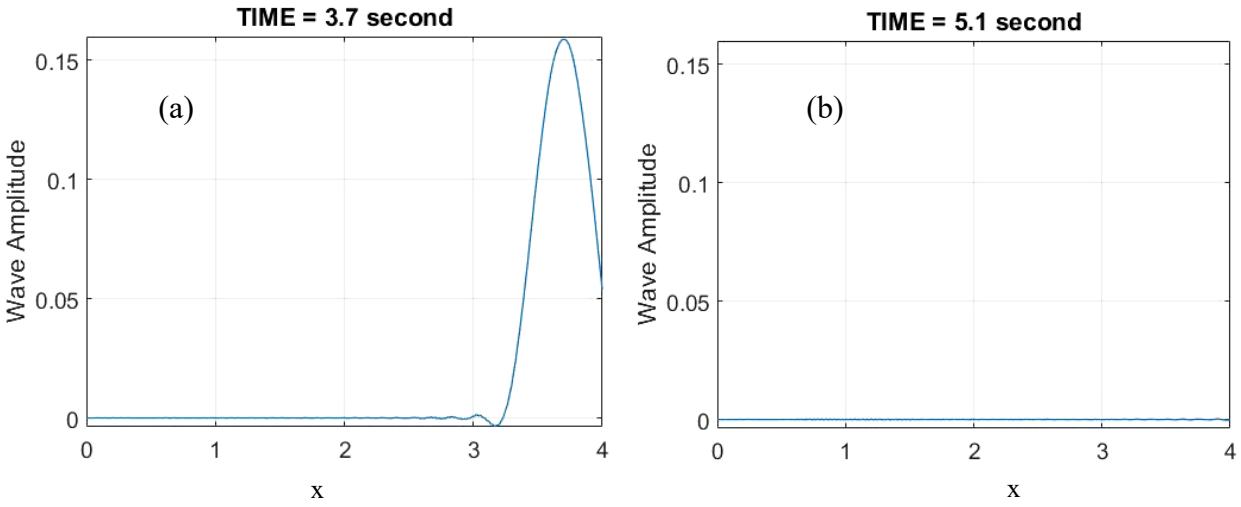

Figure 5. Wave solutions of the 1D beam with 250 nodes with the absorbing boundary condition imposed at x=4.0. (a) When the wavefront reaching the boundary and (b) after the wavefront reaching the boundary.

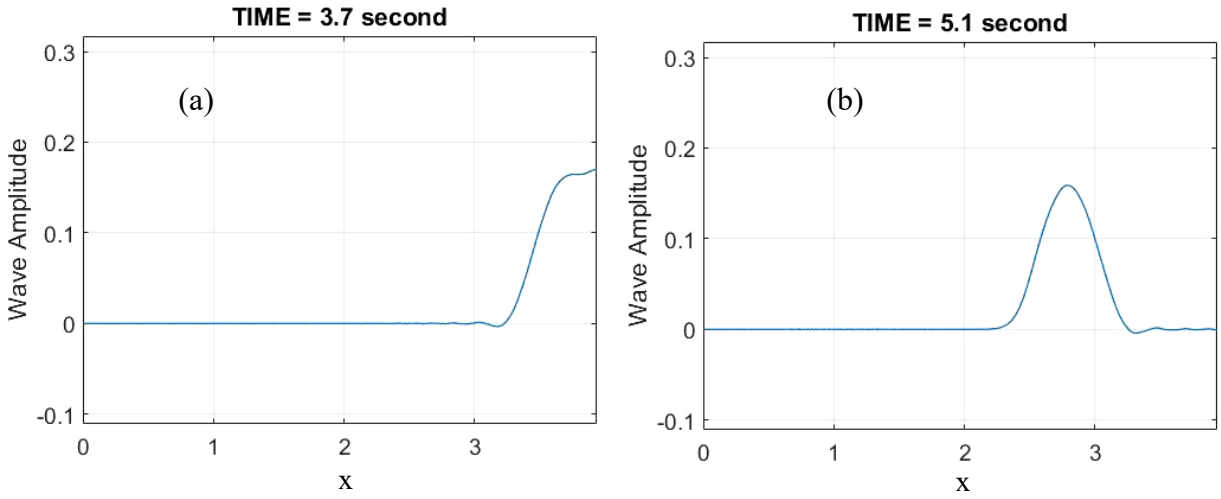

Figure 6. Wave solutions of the 1D beam with 250 nodes at different time instances with a free end at x=4. (a) When the wavefront reaching the boundary and (b) after the wavefront reaching the boundary.

Problem 2: 2D case

Consider the wave propagation problem without the body force, $E = 4 \times 10^7, \rho = 2 \times 10^3$, $Lx = 1$, $Ly = 1$, $Poisson's\ ratio = 0.2$. The initial velocity is given in the center of the square plate (Figure 7). This example was analyzed using the MSNNI method with 10000 nodes. The results in Figure 8 and Figure 9 show that the standard viscous boundary absorbs the impinging waves considerably but some small amount of waves is reflected in the solution domain. This is due to the waves hitting at an angle of more than 30°. Nonetheless, the absorbing result is satisfactory considering the percentage of reflected energy to the inserting energy. In contrast, without absorbing boundary, the reflected wave has an adverse effect on the solution.

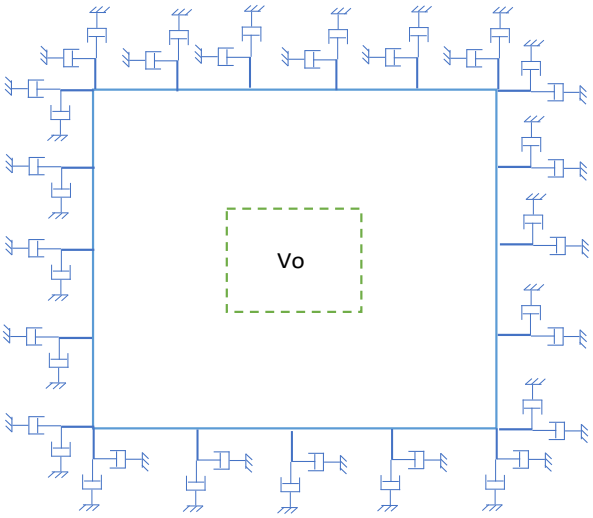

Figure 7. Schematic of a 2D block with dampers on the boundary

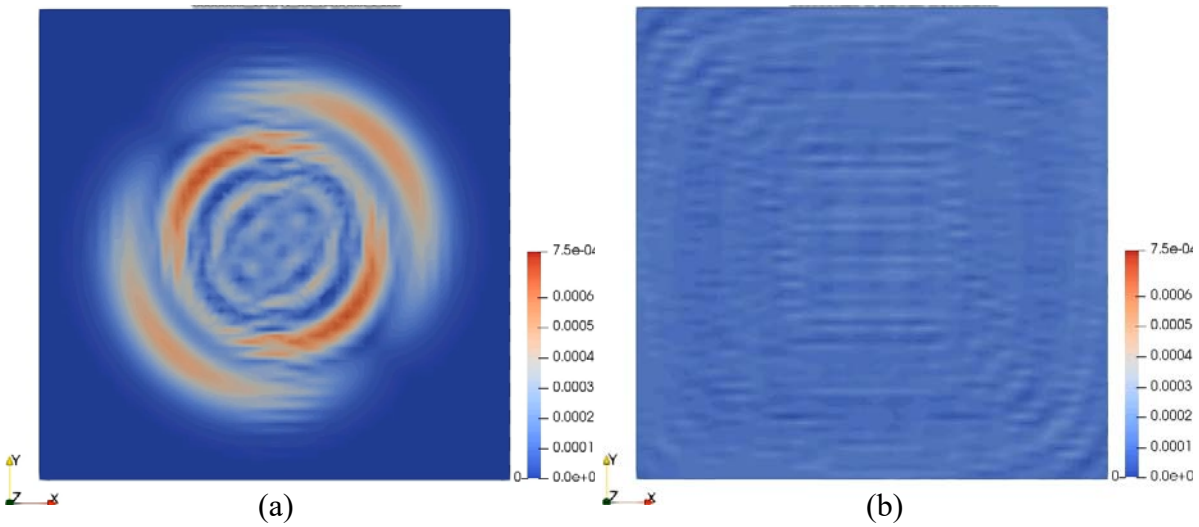

Figure 8. Wave solutions of the 2D block at different time instances with the absorbing boundary condition at the perimeter. (a) Before the wavefront reaching the boundary and (b) after the wavefront reaching the boundary.

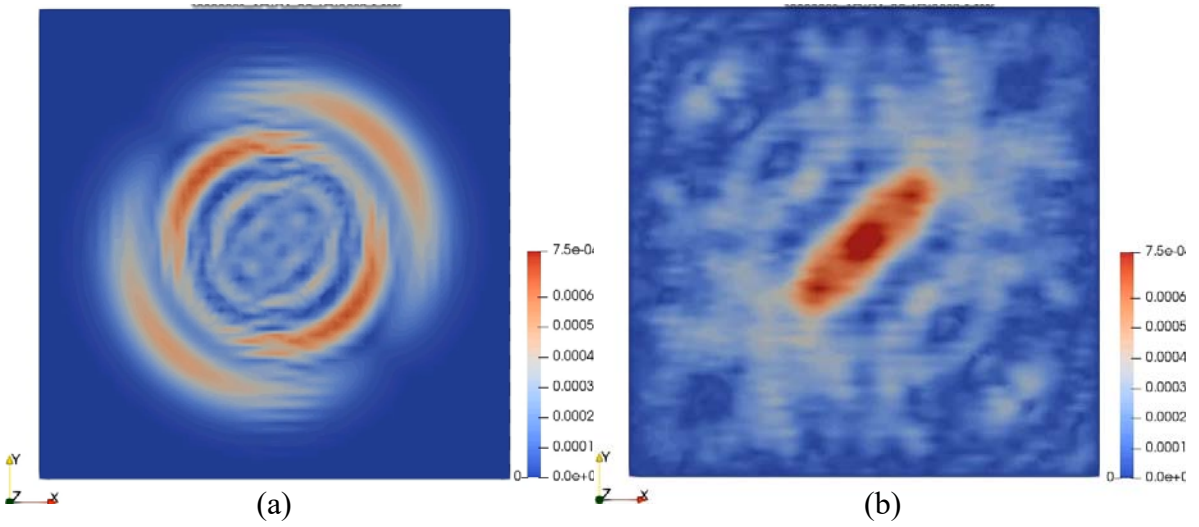

Figure 9. Wave solutions of the 2D block at different time instances with the fixed boundary at the perimeter. (a) Before the wavefront reaching the boundary and (b) after the wavefront reaching the boundary.

Problem 3: 3D case

Consider the wave propagation problem with a pressure load at the center of the top surface. $E = 4 \times 10^7, \rho = 2 \times 10^3$, $Lx = 1$, $Ly = 1$, $and\ Poisson's\ ratio = 0.2$. An impulse force is given at the top of the cube, and the wave travels from the top as shown in Figure 10. Due to the symmetry, only a quarter of the model with proper boundary conditions is constructed as shown in Figure 10.

The numerical solutions were obtained using the MSNNI method with 20402 nodes. From Figure 11 and Figure 12, with the standard viscous boundary, the incoming waves are efficiently absorbed whereas, with the fixed boundary, more disturbance in the solution appears due to reflection of the waves. However, some small spurious reflection was observed in the solution. It is known that completely absorbing a broad-spectrum wave in 3D is generally infeasible. Nonetheless, the standard viscous boundary performs well in absorbing waves without significantly disturbing the solution.

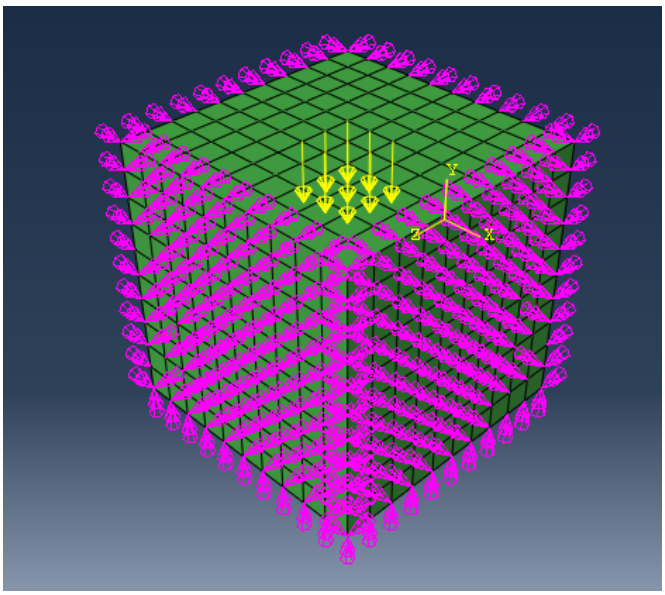

Figure 10. Schematic of the 3D cube with dampers on the boundary

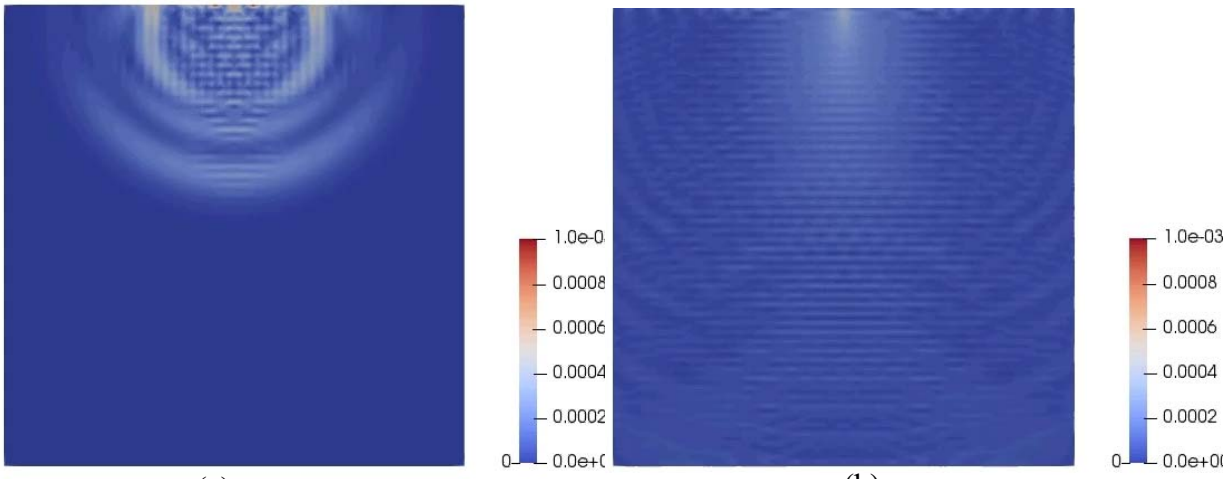

(a) (b)

Figure 11. Side view of wave solutions of the 3D cube with the absorbing boundary. (a) Before the wavefront reaching the boundary and (b) after the wavefront reaching the boundary.

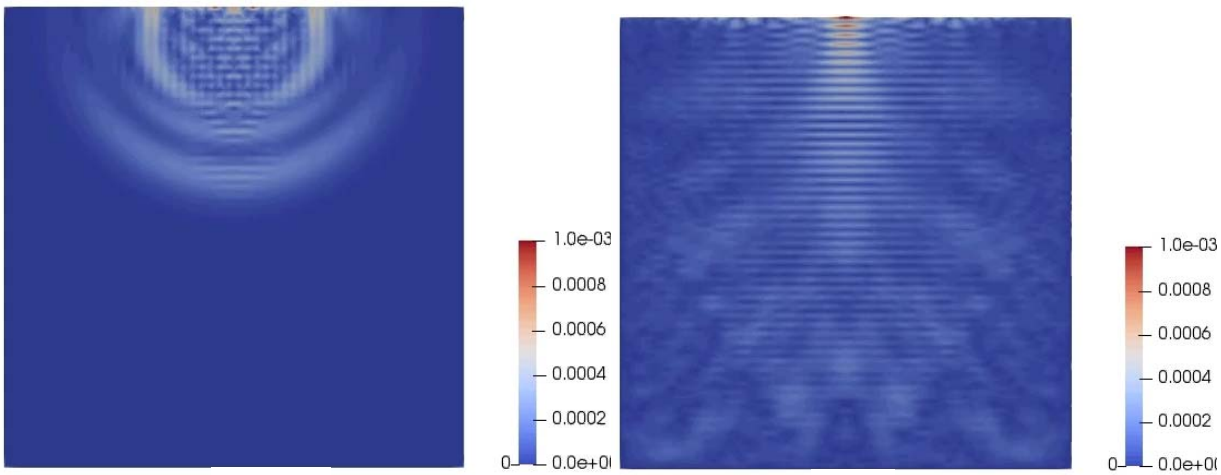

(a) (b)

Figure 12. Side view of wave solutions of the 3D cube with the fixed boundary. (a) Before the wavefront reaching the boundary and (b) after the wavefront reaching the boundary.

4.2. Task 2: Soil Constitutive Model Improvement

During this year, we have implemented some improvements to the model to more accurately capture soil behavior. We have reformulated and implemented the growth function for the cap surface so that it better reproduces experimental data (Figure 13). Previously, the shrinking of the yield surface can be seen when the cap softens. In the old cap function,

$$X(\kappa) = \kappa - RF_f(\kappa), \tag{16}$$

the size of the cap decreased as the cohesion and, hence, F_f decreased. The cap growth function is now

$$X = \hat{R}\kappa + S \tag{17}$$

which allows X to grow with κ. R and S are both constants.

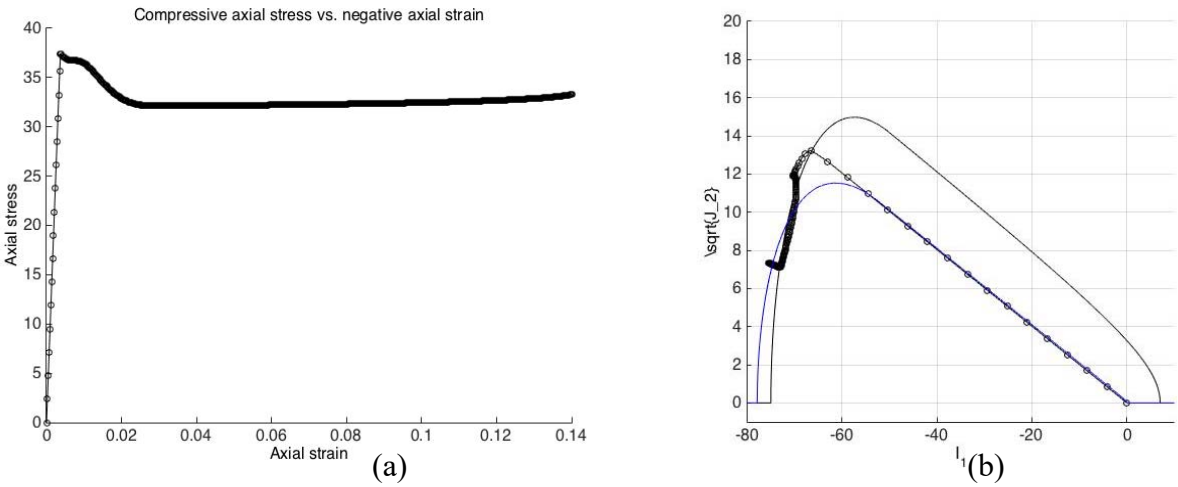

Figure 13. Triaxial compression test showing cap hardening. (a) Axial strain vs axial stress, compression positive and (b) first invariant of the stress tensor vs the square root of the second. The first invariant is three-times mean stress (tension positive), while the square root of the second invariant is a generalized measure of shear stress.

Simulations show that inelastic compaction at high mean stresses is more accurately captured. We have also split the viscosity formulation into volumetric and distortional (isochoric) parts, with different fluidity parameters. In a single fluidity Duvaut-Lions model, the stress calculation is a weighted average between the elastic trial and plastic solutions:

$$\boldsymbol{\sigma}_{n+1} = \frac{\Delta t}{\eta + \Delta t}\boldsymbol{\sigma}^{tr} + \frac{\Delta t}{\eta + \Delta t}\tilde{\boldsymbol{\sigma}} \tag{18}$$

Here, mean stress and deviatoric stress are calculated separately.

$$\begin{aligned} \mathbf{s}_{n+1} &= \frac{\Delta t}{\eta_s + \Delta t}\mathbf{s}^{tr} + \frac{\Delta t}{\eta_s + \Delta t}\tilde{\mathbf{s}} \\ p_{n+1} &= \frac{\Delta t}{\eta_p + \Delta t}p^{tr} + \frac{\Delta t}{\eta_p + \Delta t}\tilde{p} \end{aligned} \tag{19}$$

where the superscript 'tr' indicates the trial elastic component, the tilde indicates the inviscid plastic solution, η is a fluidity parameter, Δt is the time step, $\boldsymbol{\sigma}$ is the total stress, $\boldsymbol{s}$ is the deviatoric stress, and p is the mean stress. Hence the weighting uses different viscosity parameters for volumetric and shear deformation.

We have also modified the plastic potential function so that plastic compaction of the soil may occur under even as the shear strength is increasing. This behavior is more characteristic of most soils. The plastic potential is

$$g = \Gamma(\beta)\sqrt{J_2} - \sqrt{F_c^g}F_f^g \tag{20}$$

The change is in the function F_c^g , which is now

$$F_c^g = 1 - H\left(\kappa^g - I_1\right)\left(\frac{I_1 - \kappa^g}{X - \kappa^g}\right)^2 \tag{21}$$

The difference is that κ^g has replaced κ, allowing plastic compaction to occur at lower mean stresses.

We have also implemented some algorithmic improvements that enhance the robustness and efficiency of the soil model implementation. These include calculating some products, where possible, in the spectral form rather than using the full matrix. Changes to the way that the tangent modulus is calculated have improved performance and speed. Numerical testing indicates optimal quadratic convergence over a wide range of parameter values and loading conditions (Figure 14).

Compression phase

Iteration (2nd plastic step)	Local residual	Global residual
1	7.7802e-02	4.2458e-01
2	3.2648e-04	3.0628e-02
3	1.2793e-08	1.5258e-04
4	1.9133e-15	3.7684e-09

Shear phase

Iteration (2nd plastic step)	Local residual	Global residual
1	2.1246e+00	3.9544e-01
2	7.0060e-01	6.2424e-02
3	3.4995e-01	1.2914e-03
4	1.7306e-02	5.3546e-07
5	9.8324e-05	9.3265e-14
6	1.1523e-09	
7	6.8664e-16	

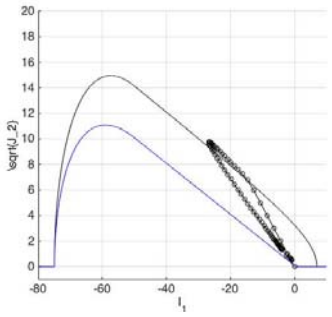

Figure 14. Local and global convergence output for a typical time step in a one-element test in combined compression and shear with the load path.

These improvements have been verified with previous versions of the model as well as simpler models such as the Drucker-Prager model (Figure 15), and the meshfree implementation matches the finite element for prescribed displacement (Figure 16). They are better at reproducing soil behavior than before. There are still some ongoing simulations.

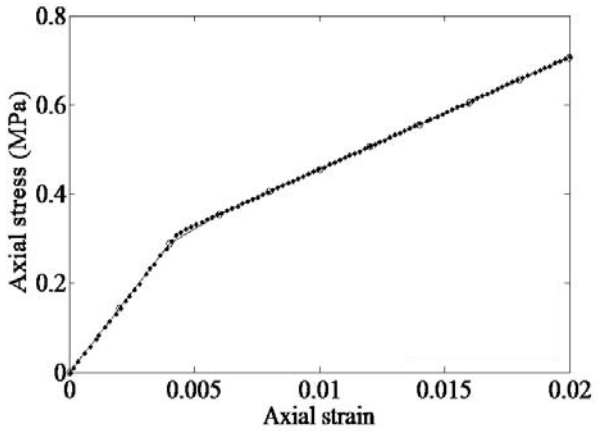

Uniaxial compression

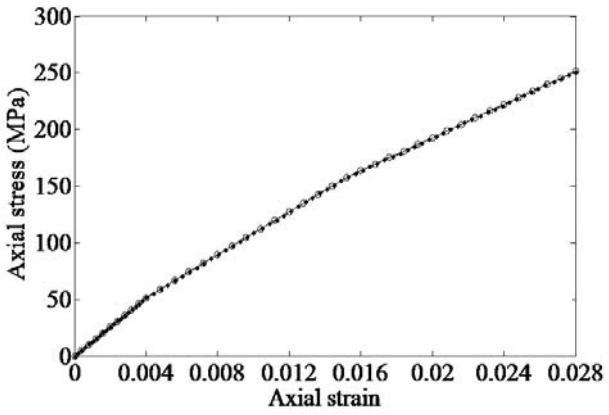

Triaxial compression

Figure 15. Verification of the current model vs. Drucker-Prager model when the parameters match

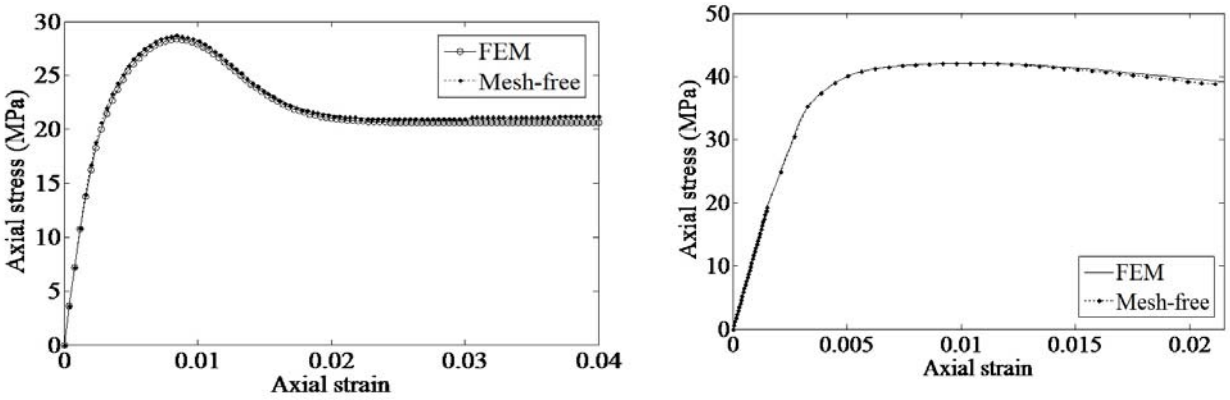

Figure 16. Verification between the meshfree and finite element implementations of the model. Slight difference can be attributed to the fact that the meshfree code is dynamic, while the finite element code is quasi-static.

4.3. Task 3: Soil Tests and Drop Tests for Dry Sand

In this reporting period, we select silica sand (natural grain) as the soil material to verify and validate the calibration and simulation procedures.

4.3.1. Soil Tests for Parameter Calibration of Dry Sand

Silica sand from U.S. Silica Company (Figure 17) was selected as the target in the dry test. Its mechanical properties were determined by the following soil experiments, including density determination, specific gravity determination by pycnometer, the grain size analysis, and the Unconsolidated Undrained triaxial test (UU).

Figure 17. Dry sand sample – silica sand (natural grain)

Density (Unit Weight) Determination:

The goal of this measurement is to determine the lab density of an undisturbed sand sample obtained by filling the sand sample into a thin-walled cylinder. The dry density is the ratio of the dry soil to the total sample volume. According to ASTM D2937-10 standard test for the density of soil in the lab by the Drive-Cylinder Method, the same test was repeated six times to determine the density of the sand. Table 1 shows the test data and the mean density of the sand sample is 1.70 g/cm^3.

Table 1. Experimental results of density for the sample sand

Test No.	M_c	M_{cs}	M_t	ρ_d
1	746.6	850	103.4	1.703
2	746.5	852.3	105.8	1.742
3	746.5	849.8	103.3	1.701
4	557.2	659.5	102.3	1.685
5	557.2	660.5	103.3	1.701
6	557.2	659.6	102.4	1.686
			Average	1.70

where

Length of Soil Sample, L(cm)	7.059
Diameter of Soil Sample, D(cm)	3.310
Volume, V(cm^3)	60.725
Mass of Empty, Clean, Dry Can, (g)	M_c
Mass of Can, Lid, and Dry Soil, (g)	M_{cs}
Mass of Dry Soil Sample, (g)	M_t
Dry Density, (g/cm^3)	ρ_d

Specific Gravity Determination by Pycnometer:

The goal of this measurement is to determine the specific gravity of the sand sample. Specific gravity is the density of the soil solids at a stated temperature divided by the density of water at the same temperature. According to ASTM D854-00 standard test for specific gravity of soil solids

by water pycnometer, the specific gravity of the sand was determined by the average of two repeated experiments. The results are shown in Table 2, and the specific gravity determined is 2.72.

Table 2. Experimental results of specific gravity for sample sand

Specimen Number	1	2
Pycnometer Bottle Number	6	120
M_p	48.8	47.5
M_{ps}	59.7	62.7
M_b	153.7	156.4
M_a	146.8	146.8
G_s	2.725	2.71
Average G_s	2.72	
M_o	10.9	15.2

where

Mass of the Oven-dry Soil Sample, (g)	$M_o = M_{ps} - M_p$
Mass of Empty, Clean Pycnometer, (g)	M_p
Mass of Empty Pycnometer and Dry Soil, (g)	M_{ps}
Mass of Pycnometer, Dry Soil, and Water, (g)	M_b
Mass of Pycnometer and Water, (g)	M_a
Specific Gravity of Soils	G_s

Above the specific gravity of the sand G_s was obtained using $G_s = \frac{M_0}{M_0 + M_a - M_b}$.

Grain Size Analysis - Sieve and Hydrometer Analysis:

This measurement is to determine the distribution of grain sizes in the sand sample. The larger particles were separated by sieve analysis, and the finer ones were tested using a hydrometer. According to ASTM D422 - standard test method for particle-size analysis of soils, totally 450.2 g sand was sieved by the sieve shaker for 10 minutes in the set of sieves. The size distribution is

showing in Table 3 and Figure 18. From the sieve analysis, the size distribution was determined as gravel: 0.00%, Sand: 99.98%, and Fines: 0.02%. The results show that the sample sand is pure sand, and therefore further hydrometer analysis for the fines part is not needed.

Unconsolidated Undrained Triaxial Test (UU)

The Unconsolidated Undrained Triaxial Test (UU) was conducted to determine the shear strength parameters of the sand sample. In this test, the sand sample is not allowed to consolidate at any time. The test simulates rapid loading with no time for settling. According to ASTM D2850, there are a few changes to meet the project's needs. Under 15-psi confining pressure, two deformation speeds (1% and 10% of strain per minute) were applied to obtain stress-strain relationships.

A cylindrical specimen (diameter: 70.000 mm and height: 122.9mm) using the specific membrane was assembled on the triaxial base cell as shown in Figure 19. The triaxial cell was filled with water and the compression was applied on the top of the cylindrical specimen. The measurement was carried on using the displacement-controlled setting at two deformation speeds, i.e., 1% and 10% strain per minute. Vertical load and displacement were recorded until the sample failure was noticed. The data are given in Tables 4 and 5, and Figure 20 and Figure 21 show the stress-strain relationship representing the failure behavior of sample sand. The average angle of friction is 34.23°.

Table 3. Experimental results of grain size analysis for the sample sand

Sieve Number	Diameter (mm)	Mass Empty Sieve (g)	Mass Sieve & Soil Retained (g)	Mass Soil Retained (g)	Percent Retained	Percent Passing
4	4.75	516.6	516.6	0	0.00	100.00
10	2	659.9	659.9	0	0.00	100.00
20	0.85	454.2	456.9	2.7	0.60	99.40
40	0.425	372.6	793.2	420.6	93.45	5.95
60	0.25	366.1	392.1	26	5.78	0.18
140	0.106	345.1	345.7	0.6	0.13	0.04
200	0.075	315.8	315.9	0.1	0.02	0.02
pan	0	374.5	374.6	0.1	0.02	0.00
			Total (g)	450.1		

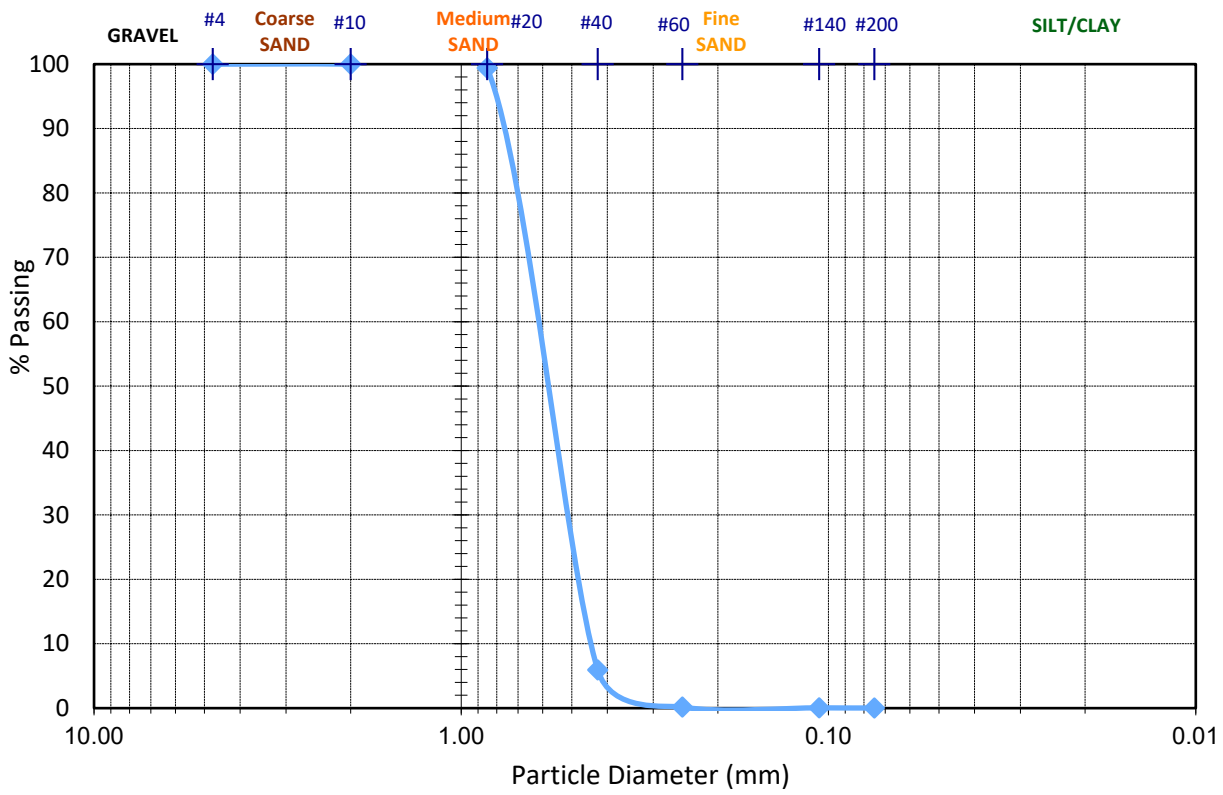

Figure 18. Grain size vs. percent finer for the sample sand

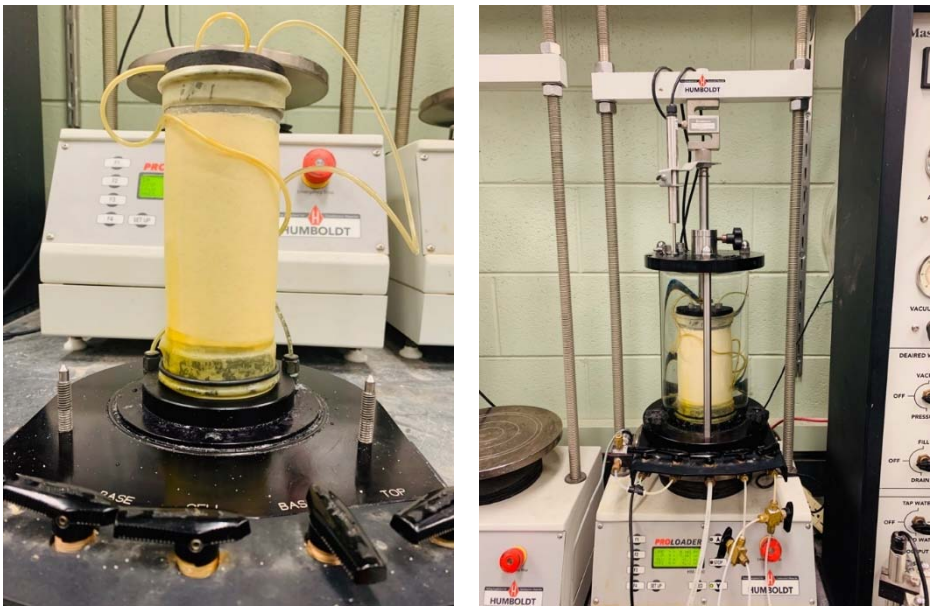

Figure 19. The sample sand specimen (left) and the test equipment before filling in water (right)

Table 4. Experimental results of unconsolidated undrained triaxial test (UU) for the sample sand (loading speed 1.3 mm/min)

Test 1		Test 2		Test 3	
Strain	Stress (kPa)	Strain	Stress (kPa)	Strain	Stress (kPa)
0	0.7788	0.0000	2.5961	0.0000	24.1433
0.0013	1.2980	0.0005	157.0614	0.0001	133.1777
0.0029	116.8225	0.0021	280.1144	0.0007	187.9545
0.0044	225.5973	0.0036	346.3139	0.0020	251.8174
0.0060	274.4031	0.0051	374.6109	0.0035	297.5080
0.0076	309.4499	0.0069	389.1488	0.0051	332.8144
0.0093	340.3429	0.0086	395.6389	0.0067	358.7749
0.0109	363.9671	0.0103	400.3118	0.0085	380.3222
0.0126	382.6587	0.0121	402.6483	0.0100	397.9754
0.0143	401.0907	0.0138	402.9079	0.0118	413.0325
0.0160	414.8498	0.0155	403.6867	0.0134	423.9360
0.0177	424.7148	0.0172	404.9847	0.0151	434.0606
0.0195	432.2433	0.0189	406.2828	0.0169	441.0699
0.0211	437.9547	0.0207	407.3212	0.0186	447.3005
0.0230	440.5507	0.0224	408.1000	0.0203	451.7138
0.0248	443.9256	0.0243	409.3980	0.0221	455.3482
0.0265	446.2620	0.0260	410.1769	0.0237	458.4635
0.0283	448.8581	0.0278	409.9172	0.0257	459.7615
0.0300	450.9349	0.0295	409.6576	0.0274	462.0980
0.0319	451.4541	0.0314	408.1000	0.0291	464.9536
0.0336	451.4541	0.0331	408.6192	0.0308	467.2901
0.0355	451.4541	0.0348	406.5424	0.0326	468.3285
0.0371	450.6753	0.0366	404.7251	0.0344	468.0689
0.0388	450.9349	0.0384	403.1675	0.0361	467.2901
0.0407	450.4157	0.0401	401.6099	0.0379	465.7325

0.0425	449.8965	0.0420	400.0522	0.0413	464.9536
0.0443	449.1177	0.0439	397.1966	0.0448	464.1748
0.0460	447.8197	0.0456	396.6774	0.0482	461.8384
0.0477	447.0409	0.0474	394.6005	0.0520	457.9443
0.0513	446.0024	0.0510	389.6680	0.0555	454.5694
0.0547	443.9256	0.0544	386.5527	0.0590	450.4157
0.0583	442.1083	0.0578	384.7355		
0.0618	439.7719	0.0613	381.6202		
0.0653	439.2527				
0.0688	437.1758				
0.0723	431.2049				
0.0736	412.5133				
0.0736	410.6961				
0.0736	409.3980				

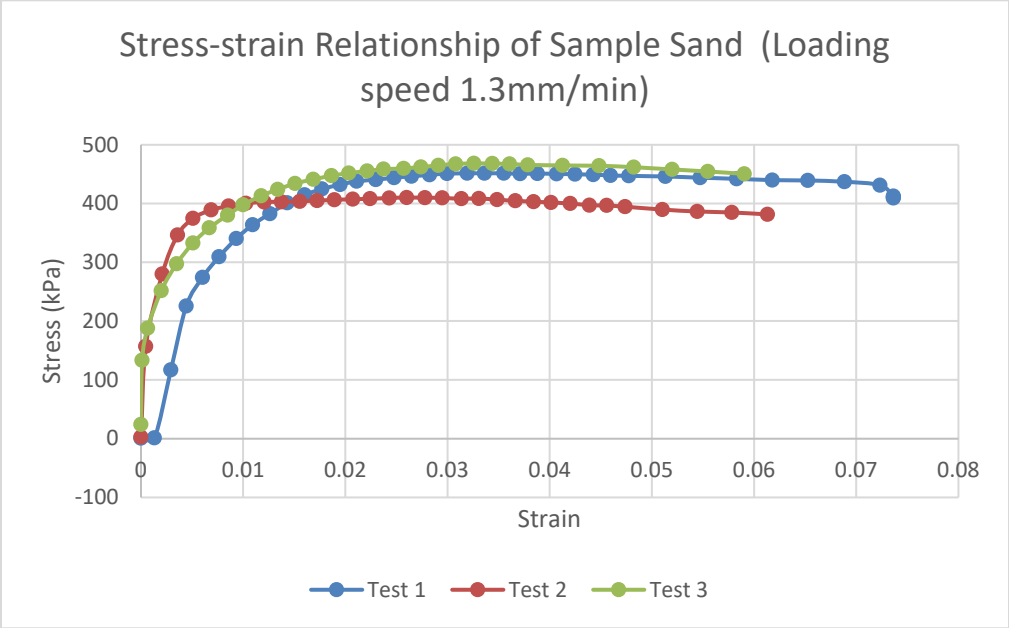

Figure 20. Stress-strain relationship of the sample sand (loading speed 1.3 mm/min)

Table 5. Experimental results of unconsolidated undrained triaxial test (UU) for the sample sand (loading speed 13 mm/min)

Test 1		Test 2		Test 3	
Strain	Stress (kPa)	Strain	Stress (kPa)	Strain	Stress (kPa)
0.0000	97.2312	0.0000	11.6989	0.0000	3.1197
0.0008	190.5628	0.0020	278.6949	0.0023	304.9526
0.0031	271.6755	0.0108	359.2877	0.0057	375.9262
0.0039	285.1943	0.0204	389.1850	0.0093	413.1028
0.0076	314.0517	0.0290	400.8839	0.0130	434.6809
0.0101	360.3276	0.0381	407.3833	0.0173	446.6398
0.0120	371.5066	0.0462	407.1234	0.0219	452.6193
0.0158	392.0447	0.0543	405.8235	0.0303	454.4391
0.0162	400.6239	0.0635	404.7836	0.0354	453.1392
0.0236	416.4825	0.0730	403.2237	0.0399	452.8792
0.0289	423.7619	0.0818	399.3241	0.0489	455.7390
0.0336	427.1416	0.0900	398.2842	0.0532	452.6193
0.0379	428.1815	0.0993	394.6445	0.0574	447.9397
0.0415	428.7014	0.1079	391.7847	0.0667	438.3206
0.0468	432.6011	0.1163	388.6650	0.0752	428.9614
0.0527	432.0811	0.1251	388.4050	0.0843	417.2624
0.0561	430.2613	0.1338	386.8452	0.0926	406.6034
0.0634	425.5817	0.1432	390.7448	0.1018	398.8041
0.0733	419.8622	0.1511	390.2249	0.1106	396.2043
0.0817	411.2830	0.1612	387.8851	0.1191	394.9045
0.0872	400.6239	0.1686	386.3252	0.1282	395.1644
0.0967	394.6445	0.1782	385.5453	0.1358	394.6445
0.1043	391.2648	0.1863	386.0653	0.1455	395.1644
0.1138	388.4050	0.1951	389.4449		
0.1222	387.3651				

0.1302	384.5054				
0.1400	384.5054				
0.1486	386.5852				
0.1653	389.9649				
0.1834	401.1439				
0.2010	417.7824				

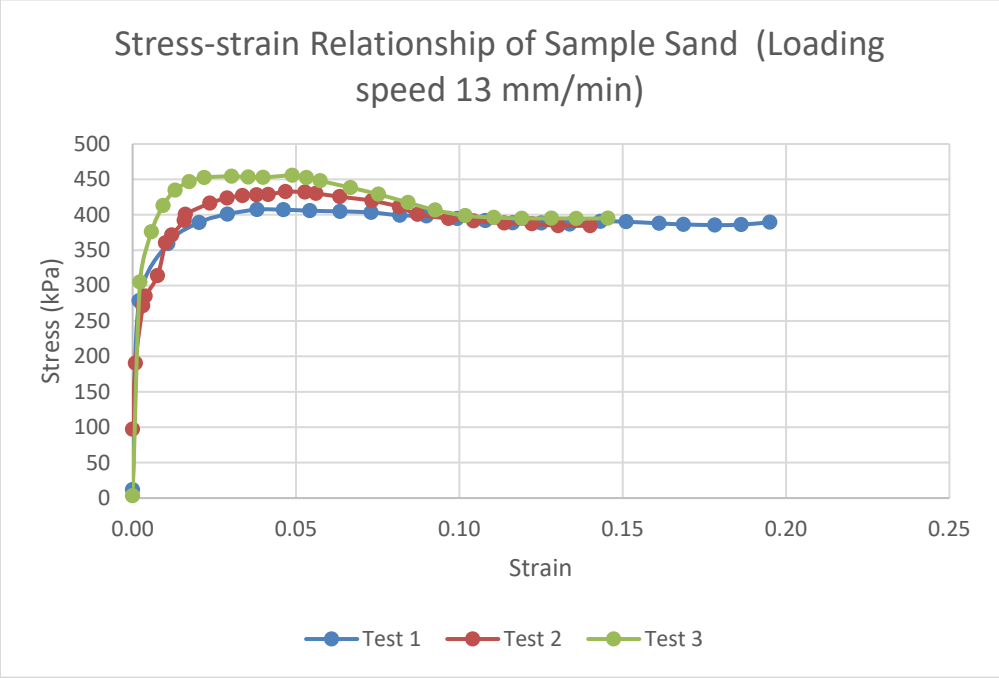

Figure 21. Stress-strain relationship of the sample sand (loading speed 13 mm/min)

4.3.2. Spherical Ball Drop Test Experiment

An experiment on a spherical ball dropped on the natural sand grain was conducted to evaluate the penetration depth of the ball into the dry sand. The ball was dropped from different heights (500 mm, 1000 mm, and 1500 mm) with variable spherical steel ball diameter, i.e., 25.4 mm, 22.23 mm, and 19.05mm. The natural grain sand was deposited in a container that has a radius of 150 mm at the top and 135 mm at the bottom and a height of 355 mm. The sand specimen contained forms a cylinder of a nominal radius of 140 mm and a height of 150 mm. The test frame is equipped with an electromagnet at the center to hold the steel ball at the desired height. The ball was dropped in such a way that it hits at the center of the cylindrical soil grain. Penetration depth was measured at the top of the steel ball, so the results shown below are the penetration depths at the top of the ball. Experimental data are given in Table 6.

Figure 22. Experimental setup of spherical steel ball penetrating the dry sand

Table 6. Spherical ball dropped from 500 mm height

Test No.	Diameter of the ball (mm)	Top of Soil (mm)	Penetration measured at the top of the ball (mm)	Penetration depth (mm)
1	25.4	35.7575	46.6875	10.93
2	22.225	34.86	48.2825	13.4225
3	19.05	35.21	47.2975	12.0875
4	15.875	35.3125	47.3275	12.015

Table 7. Spherical ball dropped from 1000 mm height

Test No.	Diameter of the ball (mm)	Top of Soil (mm)	Penetration measured at the top of the ball (mm)	Penetration depth (mm)
1	25.4	34.96	53.385	18.425
2	22.225	34.8025	56.6725	21.87
3	19.05	34.51	56.1075	21.5975
4	15.875	35.5875	56.7075	21.12

Table 8. Spherical ball dropped from 1500 mm height

Test No.	Diameter of the ball (mm)	Top of Soil (mm)	Penetration measured at the top of the ball(mm)	Penetration depth (mm)
1	25.4	31.01	57.465	26.455
2	22.225	32.1425	60.15	28.0075
3	19.05	33.6075	65.2025	31.595
4	15.875	33.53	58.9225	25.3925

4.4. Simulation Results for Model Calibration and Validation

4.4.1. Triaxial Test Simulation for Soil Property Calibration

This simulation is to verify the numerical constitutive model with the experimental data, by using the calibrated material properties and the Drucker-Prager constitutive model. A cylinder of sand grains of depth 123 mm and diameter 70 mm was constructed to compare the numerical with the experimental stress-strain graph. The model consists of 4268 nodes with lateral restraint on the circumference and fixed at the bottom (Figure 23). A displacement control was applied at the top of the cylinder. The numerical model was simulated using the meshfree code with the MSNNI method. The parameters used in the simulation were calibrated from the experiments described in Section 4.3.1 and are given in Table 9.

Table 9. Drucker-Prager parameters and properties

Drucker-Prager soil properties	
Young's modulus (E)	$6.0 \times 10^7 \frac{N}{m^2}$
Poisson's ratio (ν)	0.30
Friction Parameter (β)	0.81
	$1.0 \times 10^8 \frac{N}{m^2}$
Cohesion strength (α)	0.0
First parameter for damage accumulation function	0.05
Second parameter for damage accumulation function	1.0
Density (ρ)	$1700 \frac{kg}{m^3}$
Mass-proportional damping coefficient	0.05

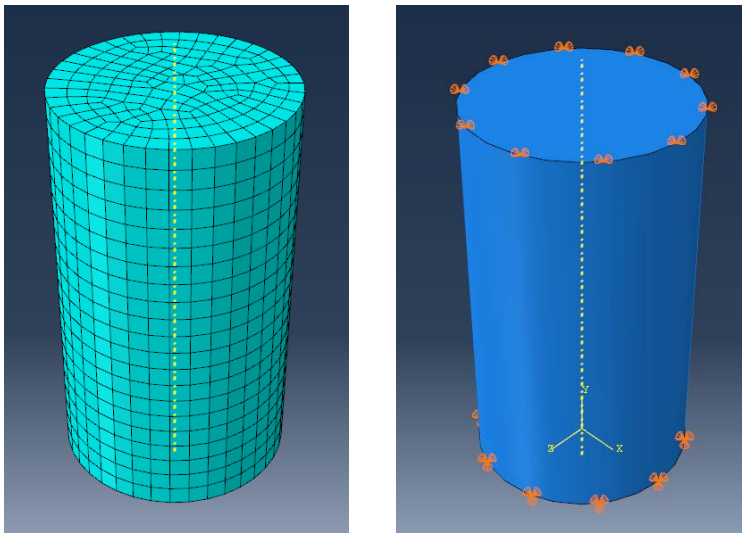

Figure 23. Mesh for the triaxial test using cylindrical grain

The model was constructed as shown in Figure 23 and proper boundary conditions were imposed to mimic the actual experimental conditions. The numerical outputs of the axial load and displacement were converted to the stress vs. strain curve to compare with the experimental data as shown in Figure 24. The numerical method reasonably agrees with the experimental data.

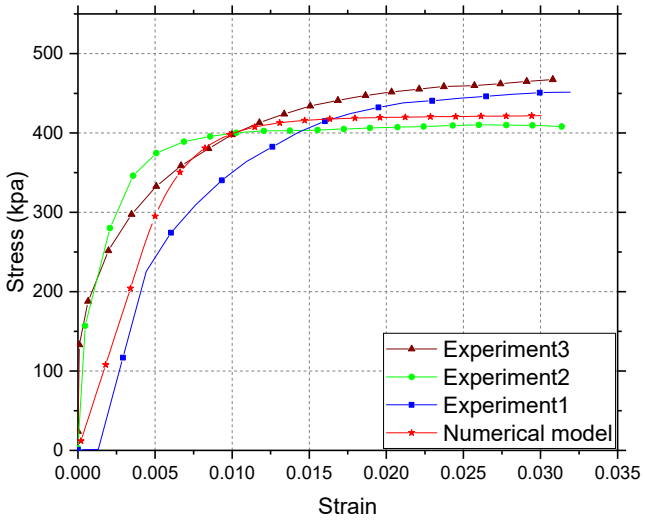

Figure 24. Stress-strain curves from experimental data and numerical simulations

4.4.2. Simulations of Spherical Ball Drop Test

To verify the numerical solution with the experimental data, a spherical ball simulation was conducted using the meshfree code. As per the experiment in the previous section, a similar type of scenario was created. A spherical steel ball was dropped from various heights, i.e., 500 mm, 1000 mm, and 1500 mm at the center of the cylindrical soil grain and then the penetration of the steel ball is measured. The soil grain was modeled using the Drucker-Prager model with the parameters as discussed in the previous section. The soil model was restrained laterally along the circumference and fixed at the bottom surface. The cylindrical soil of height 150 mm and radius 140 mm was considered. The experimental setup for this test is shown in Figure 25.

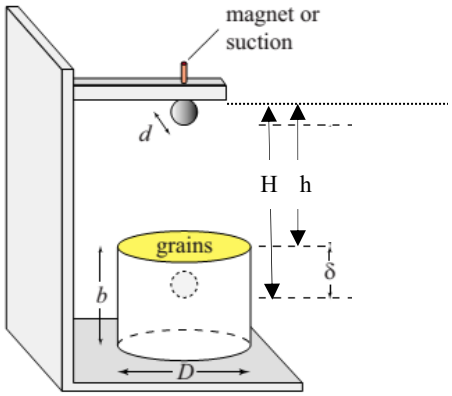

Figure 25. Experimental setup of spherical ball drop test

Variables shown in Figure 25 are described as below:

δ: Maximum penetration depth

h: Initial distance between the bottom of the sphere ball and the container surface

H: Total drop height after penetration

d: Sphere ball diameter

D: Diameter of the container ($280\ mm$ for this test)

b: Height of the container ($150\ mm$ for this test)

In this simulation, three different initial heights of $500, 1000,$ and $1500\ mm$ were tested. For computational efficiency, for all three cases, the ball was located at the distance of $50\ mm$ and corresponding initial velocities were assigned to the ball nodes for each case. For this purpose, the difference of actual total height and the assumed initial numerical height were used by the formula $v = \sqrt{2g(h - 0.05)}$, where g is the ground acceleration and v is the ball's initial vertical speed. Table 10 shows the initial velocity for three cases. The soil properties are taken from the previous

section (Table 9) and the steel-made ball linear elastic properties are as given in Table 11. An average mesh size of 4.5 mm of the hexahedral element is used for both ball and grain parts. Here the mesh configurations are shown for both parts. Figure 26 shows the mesh configuration for this model. The models were simulated using 127291 nodes with a normalized support size as 1.5 with the MSNNI method.

Table 10. Initial position and velocity for the spherical ball

Drop Height (mm)	Height Difference (mm)	Initial Velocity (mm/s)
500	450	2929.1
1000	950	4288.3
1500	1450	5310.3

Table 11. Mechanical properties of the spherical ball

Linear Elastic Material (steel ball)	
Young's modulus ($\boldsymbol{E}$)	$2 \times 10^{11}\ \frac{N}{m^2}$
Poisson's ratio ($\boldsymbol{\nu}$)	0.25
Density ($\boldsymbol{\rho}$)	$7800\ \frac{kg}{m^3}$
Mass proportional damping coefficient	0.05

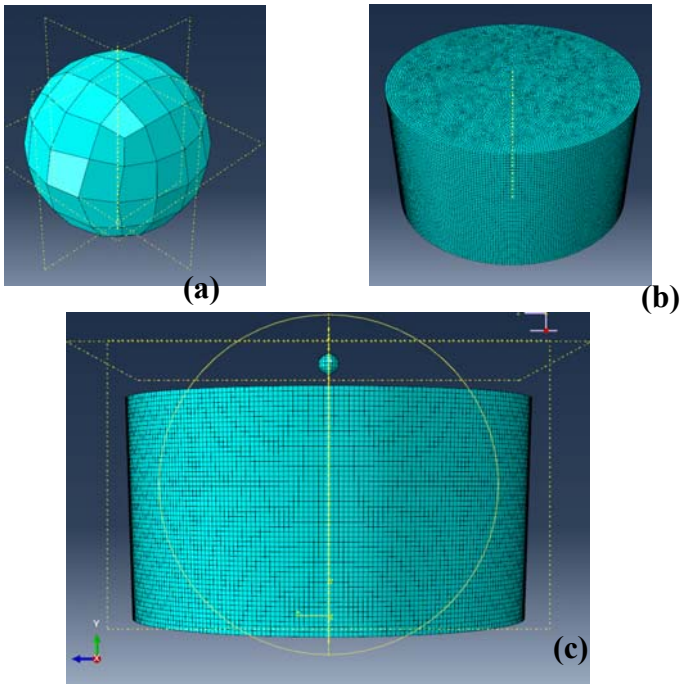

Figure 26. (a) Spherical ball mesh configuration, (b) soil grain medium mesh configuration, and (c) initial configuration in the numerical model

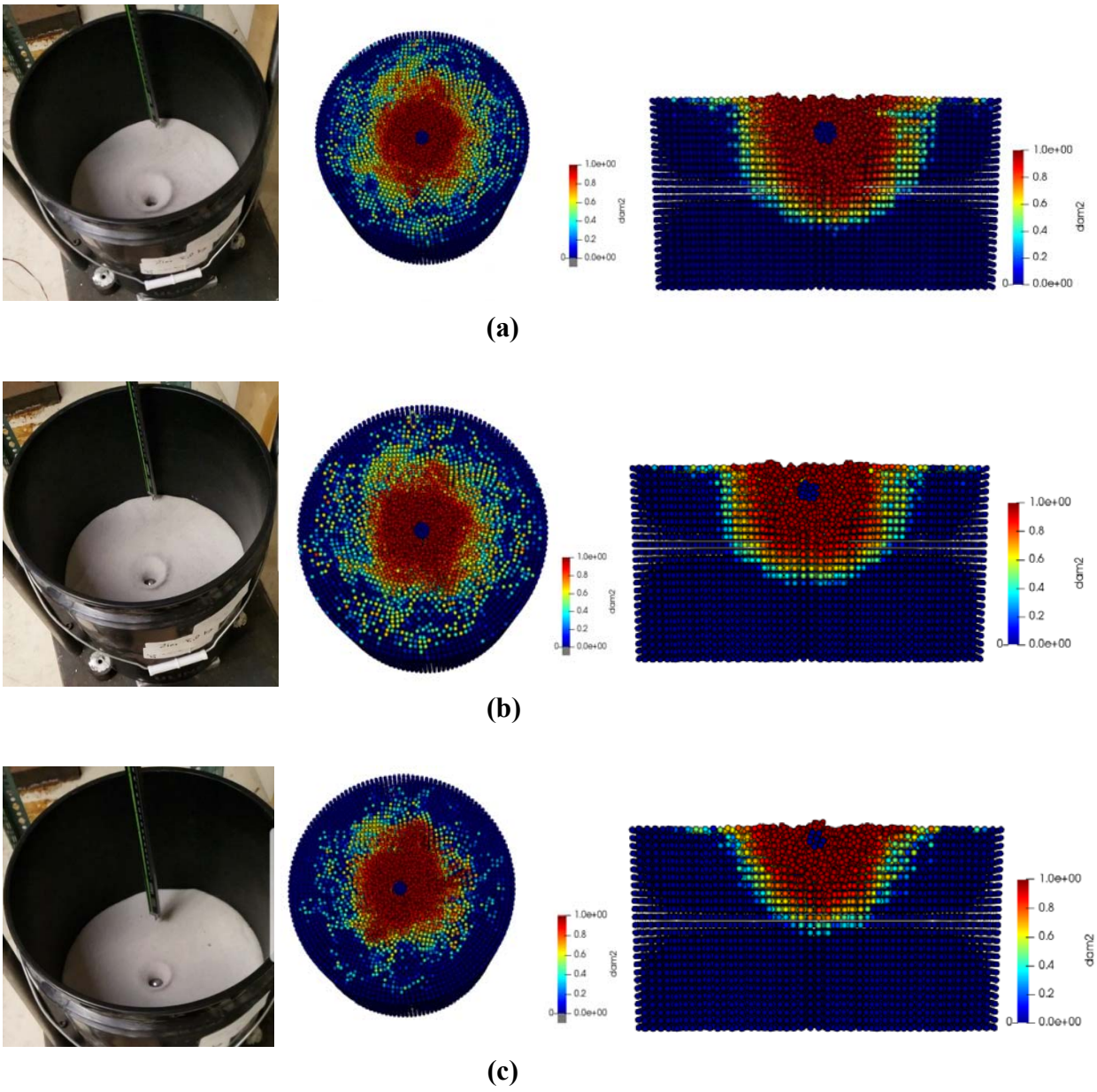

Figure 27. Comparison of numerical and experimental results with different height using a spherical ball with a 19.05-mm diameter. (a) Drop height 1500 mm, (b) drop height 1000 mm, and (c) drop height 1500 mm.

Figure 27 shows the comparison of numerical simulations and experimental results with different drop heights using the 19.05-mm diameter ball. The color contour indicates the level of damage (1 as 100% damaged). As can be seen, numerical results qualitatively capture the deformation features such as the crater size, depth, and splashing of the soil grains. Predicted penetration depth data for different ball sizes and drop heights are given in Table 12-Table 14 and the associated projectile (ball) penetration time histories are shown in Figure 28. From Tables 12-Table 14, it can be observed that as we increase the drop height, the penetration depth also increases. Also, it can be observed that the numerical results are in close agreement with the experimental result.

Table 12. Case 1: 500 mm drop height

Test No.	Size of ball (mm)	Experimental Penetration depth (mm)	Numerical Penetration depth (mm)	Error (%)
1	25.4	36.33	37.73	3.86
2	22.225	35.6475	36.81	3.26
3	19.05	31.1375	33.15	6.46

Table 13. Case 2: 1000 mm drop height

Test No.	Size of ball (mm)	Experimental Penetration depth (mm)	Numerical Penetration depth (mm)	Error (%)
1	25.4	43.825	45.62	4.10
2	22.225	44.095	43.54	1.26
3	19.05	40.6475	42.22	3.87

Table 14. Case 3: 1500 mm drop height

Test N0.	Size of ball (mm)	Experimental Penetration depth (mm)	Numerical Penetration depth (mm)	Error (%)
1	25.4	51.855	55.52	7.07
2	22.225	50.2325	53.42	6.35
3	19.05	50.645	53.08	4.81

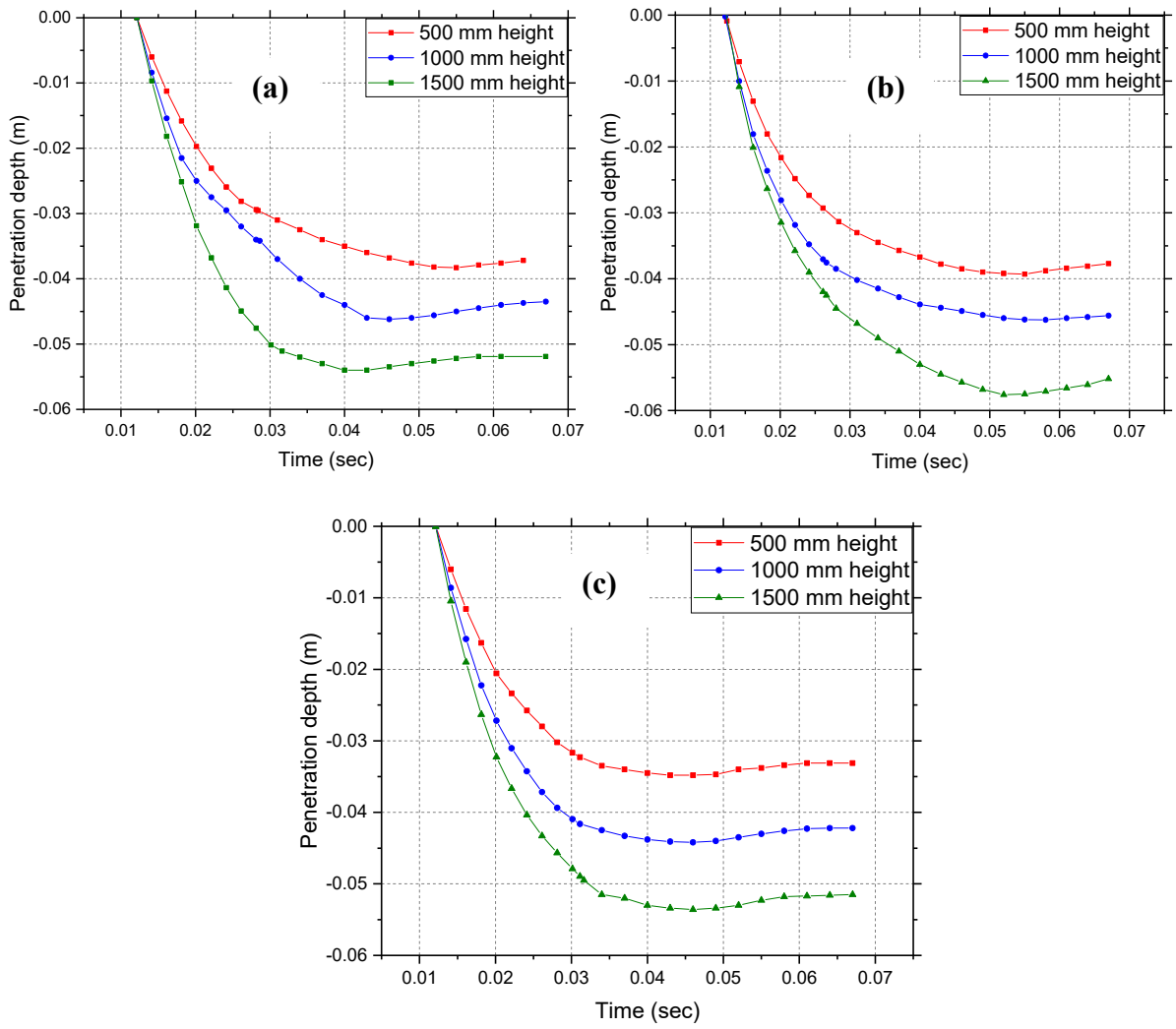

Figure 28. Projectile time histories of different drop heights. (a) Diameter 25.4 mm, (b) diameter 22.23 mm, and (c) diameter 19.05 mm.

4.4.3. Rebound of Projectile on Sandy Soil

This example is to validate the developed framework for simulations of a projectile rebound from the soil. The results described here have been partially published in (Mahdavi et al., 2019). The problem setup was taken from (Xu, et al, 2014), where the impact of a concrete spherical projectile of diameter 50 mm on the sandy soil surface with various impact velocities v_i and incident angles θ_i is studied. The simulation results are compared and validated with the experimental data provided in (Xu, et al, 2014). The schematic configuration of the process is shown in Figure 29. The experimental data from (Xu, et al, 2014) is provided in Table 15.

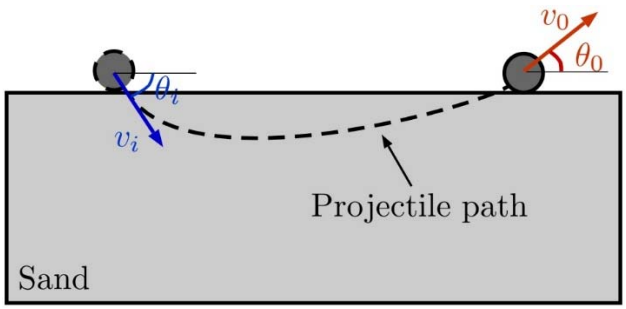

Figure 29. Schematic of ricochet of spherical projectile

Table 15. Rebound experimental data

Case No.	θ_i (°)	v_i (*m/s*)	θ_0 (°)	v_0 (*m/s*)
#1	15	61.8	12.24	45.73
#2	15	92.3	11.81	75.02
#3	30	62.23	18.72	22.51
#4	30	92.31	20.39	34.29
#5	40	52	17.17	17.09
#6	40	72.2	19.85	19.42

The material parameters were calibrated from least-squares fitting the penetration data of case No. 3. Material properties and parameters of the sand are provided in Table 16. For the concrete sphere, material properties are the same as those provided in (Xu, et al, 2014), $\rho_c = 2400\ kg/m^3$, $E_c = 8.06\times10^{10}\ Pa$ and Poisson's ratio $\nu = 0.18$. The number of nodes used to simulate the problem for all cases is 79467, whereas the normalized support size for semi-Lagrangian RKPM is considered as 1.5.

Table 16. Sand material properties and damage parameters

Granular sandy soil properties and parameters	Values
Young's Modulus (E)	40 *MPa*
Poisson's Ratio (v)	0.28
Friction Angle (φ)	35^o
Dilatancy angle (ψ)	5^o
Damage Parameter: Initiation, c_2	0.03
Damage Parameter: Critical, c_1	1.0
Density (ρ)	1724 kg/m^3

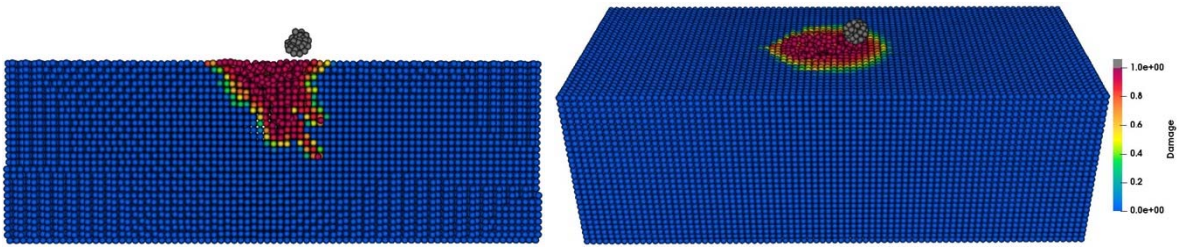

(a) (b)

Figure 30. Soil deformation and damage contours for the case with $\theta_i = 30^o$ and $v_i = 62.23$ m/s . (a) x − y cut-plane and (b) top view.

Figure 30a and Figure 30b show the soil deformation and damage contours for case No. 3 from the top and $x-y$ cut plane views, respectively, immediately after the projectile bounces back from the soil surface. After calibrating the material properties and parameters, all cases were solved and rebound angles and velocities were recorded and compared with the experimental results, as shown in Table 17. From the provided results, it is noted that the difference in outgoing velocities v_o between numerical and experimental results is more than those for the bouncing-back angles; however, the general trends in errors for both variables are almost consistent.

Table 17. Results and errors from the semi-Lagrangian RK model

Case No.	θ_0 (°)	$v_0(m/s)$	θ_0 Error (%)	v_0 Error (%)
#1	11.7	42.1	4.4	7.9
#2	11.3	68.1	4.3	9.2
#3	18.5	20.8	1.2	7.6
#4	19.1	29.9	6.3	12.8
#5	16.7	15.2	2.7	11.1
#6	18.8	17.1	5.3	11.9

The kinetic energy loss for the cases with lower impact angles (θ_i) is observed to be less than the cases with higher impact angles (larger v_i / v_o), as expected. This is justifiable by comparing the damage zone areas between the two cases (Figure 30 and Figure 31), where although case No. 2 impacts soil with higher velocity compared to the other two cases, the damaged area is considerably smaller. This agrees with the results reported in (Xu, et al, 2014).

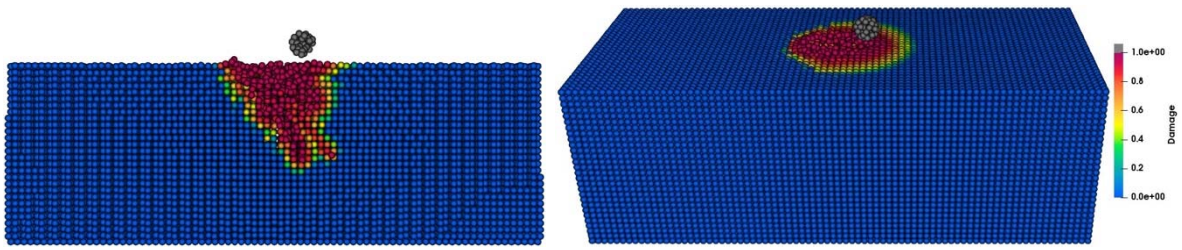

(a) (b)

Figure 31. Soil deformation and damage contours for $\theta_i = 40^o$ case and $v_i = 52$ m/s. (a) x − y cut-plane and (b) top view.

5. Proposed Second-Year Plan

Tasks	Start date	Due Date
Task 1. Enhancement of Multi-field Meshfree Code		
1.1. Pressure projection for the saturated formulation	9/1/2019	1/31/2020
1.2. Partially saturated formulation	12/1/2019	5/30/2020
1.3. Verification for the development and implementation in Tasks 1.1 and 1.2	4/1/2020	7/30/2020
1.4. Absorbing boundary condition improvement	11/1/2019	2/30/2020
Task 2. Soil Constitutive Model Improvement		
2.1. Develop material constant calibration strategy	12/1/2019	3/31/2020
2.2. Sensitivity analysis	12/1/2019	6/30/2020
2.3. Partially saturated soil model	9/1/2019	3/31/2020
2.4. Algorithm improvement and verification of Task 2.3	4/1/2020	9/30/2020
Task 3. Soil Tests and Drop Tests for Saturated Soil		
3.1. Tests for calibration of soil properties	11/1/2019	3/31/2020
3.2. Drop test for saturated soil	12/1/2019	4/30/2020
3.3. Validation for saturated soil	2/1/2020	9/30/2020
3.4. Validation for higher speed penetration	1/1/2020	5/31/2020

6. References

Chen, J.S., Hillman, M., and Chi, S.W., "Meshfree Methods: Progress Made after 20 Years," Journal of Engineering Mechanics, 2017, 2017. 143(4): p. 04017001.

Chen, J.S., Wu, C.T., Yoon, S., and You, Y., 2001. A Stabilized Conforming Nodal Integration for Galerkin Meshfree Methods. *International Journal for Numerical Methods in Engineering*, 50, 435-466.

Chen, J.S., Wu, C.T., Yoon, S., and You, Y., 2002. Nonlinear Version of Stabilized Conforming Nodal Integration for Galerkin Meshfree Methods, *International Journal for Numerical Methods in Engineering*, 53, 2587-2615.

Chen, J.S., W. Hu, M. Puso, Y. Wu, and X. Zhang, *Strain Smoothing for Stabilization and Regularization of Galerkin Meshfree Method.* Lecture Notes in Computational Science and Engineering, 2006. **57**: p. 57-76.

Chen, J.S., M. Hillman, and M. Ruter, *An arbitrary order variationally consistent integration for Galerkin meshfree methos.* International Journal for Numerical Methods in Engineering, 2013. **95**(5): p. 387-418.

Chi, S.W., Lee, C.H., Chen, J.S., and Guan, P.C., A level set enhanced natural kernel contact algorithm for impact and penetration modeling, International Journal for Numerical Methods in Engineering, 2015. 102(3):839-866.

Khan, M., *Mechanics of projectile penetration into non-cohesive soil targets*. Vol. 13. 2015. 28-39.

Mahdavi, A., Chi, S.W., and Atif, M.M., "A two-field semi-Lagrangian reproducing kernel model for impact and penetration simulation into geo-materials," Computational Particle Mechanics, 2019. https://doi.org/10.1007/s40571-019-00253-0

Wu, C.T., Chi, S.W., Koishi, M., and Wu, Y., "Strain gradient stabilization with dual stress points for the meshfree nodal integration method in inelastic analyses," International Journal for Numerical Methods in Engineering, 2016. 107(1), pp. 3-30.

Yreux, E. and Chen, J.S., A quasi-linear reproducing kernel particle method, International Journal for Numerical Methods in Engineering, 2017. 109:1045-1064.

Xu, J., et al., *A study on the ricochet of concrete debris on sand.* International Journal of Impact Engineering, 2014. **65**: p. 56-68.